Journal of Instrumentation

PAPER

Double-GEM based thermal neutron detector prototype

Published by IOP Publishing for Sissa Medialab

Received: *May 17, 2022*
Revised: *July 5, 2022*
Accepted: *July 20, 2022*
Published: *September 13, 2022*

Double-GEM based thermal neutron detector prototype

L.A. Serra Filho,[a,*] **R. Felix dos Santos,**[a] **G.G.A. de Souza,**[a] **M.M.M. Paulino,**[a] **F.A. Souza,**[b] **M. Moralles,**[b] **H.N. da Luz,**[c] **M. Bregant,**[a] **M.G. Munhoz,**[a] **C.-C. Lai,**[d,e] **C. Höglund,**[d,f,1] **P.-O. Svensson,**[d] **L. Robinson**[d] **and R. Hall-Wilton**[d,g]

[a] *Instituto de Física da Universidade de São Paulo,*
Rua do Matão 1371, Cidade Universitária 05508-090, São Paulo, Brasil
[b] *Instituto de Pesquisas Energéticas e Nucleares,*
Avenida Lineu Prestes 2242, Cidade Universitária 05508-000, São Paulo, Brasil
[c] *Institute of Experimental and Applied Physics, Czech Technical University in Prague,*
Husova 5, Prague 1 110 00, Czech Republic
[d] *Detector Group, European Spallation Source ERIC (ESS), European Spallation Source ERIC (ESS),*
P.O. Box 176, Lund 221 00, Sweden
[e] *Linköping University, Linköping University,*
Linköping 581 83, Sweden
[f] *Impact Coatings AB,*
Westmansgatan 29G, Linköping 582 16, Sweden
[g] *Università degli Studi di Milano-Bicocca,*
Piazza della Scienza 3, Milano 20126, Italy

E-mail: lserra@if.usp.br

Abstract: The Helium-3 shortage and the growing interest in neutron science constitute a driving factor in developing new neutron detection technologies. In this work, we report the development of a double-GEM detector prototype that uses a $^{10}B_4C$ layer as a neutron converter material. GEANT4 simulations were performed predicting an efficiency of $(3.14 \pm 0.10)\%$, agreeing within $2.7\,\sigma$ with the experimental and analytic detection efficiencies obtained by the detector when tested in a 41.8 meV thermal neutron beam. The detector is position sensitive, equipped with a 256+256 strip readout connected to resistive chains, and achieves a spatial resolution better than 3 mm. The gain stability over time was also measured with a fluctuation of about $0.2\%\,h^{-1}$ of the signal amplitude. A simple data acquisition with only 5 electronic channels is sufficient to operate this detector.

Keywords: Neutron detectors (cold, thermal, fast neutrons); Micropattern gaseous detectors (MSGC, GEM, THGEM, RETHGEM, MHSP, MICROPIC, MICROMEGAS, InGrid, etc); Gaseous detectors

ArXiv ePrint: 2205.07122v3

[1] Current affiliation.
[*] Corresponding author.

https://doi.org/10.1088/1748-0221/17/09/P09018

2022 JINST 17 P09018

Contents

1 Introduction **1**

2 Experimental setup **2**

3 Results and discussion **5**

3.1 Position calibration and resolution 5

3.2 Detector efficiency and gain stability 8

3.2.1 Analytic calculation 8

3.2.2 Simulations 10

3.2.3 Experimental measurements 10

4 Final considerations **13**

2022 JINST 17 P09018

1 Introduction

Several advances in scattering techniques inspired the interest in neutron science, which provides different applications in areas such as chemistry, physics, biology, medicine and engineering research. These advances are strongly dependent on detector developments, which has also grown in the last years, along with the capability to obtain bright monochromatic neutron sources, whether in large or small facilities [1–4].

The ^{3}He proportional counter is one of the most important types of neutron detectors, still widely used. Beyond its historical tradition, it presents several advantages, such as the large neutron capture cross-section (σ = 5325 b for 25 meV [5]), low sensitivity to gamma-rays, and the possibility of working on a wide neutron energy range within the low energy region [1]. However, due to a shortage of this gas since the early 2000s [6], the scientific community keeps searching for alternative solutions with ^{3}He-free detectors [7], employing ^{113}Cd, ^{157}Gd, ^{10}B, and ^{6}Li [8–12] as neutron converters. Nevertheless, substituting ^{3}He has the drawback of reducing the neutron detection efficiency or increasing the detection complexity.

One versatile alternative for neutron detection consists of using one of the referred neutron converter isotopes with the Gas Electron Multiplier (GEM) [13], a microstructure widely used to detect charged particles that can cover large sensitive areas, present fair energy and position resolutions as well as robustness. These aspects consolidated these microstructures, which are already in use in several applications, such as high energy physics [14–16], muon tomography [17], X-rays fluorescence imaging [18], and, more recently, neutron detection [19–22].

This work presents a double-GEM detector which uses $^{10}B_4C$ as a neutron converter, deposited on its aluminum cathode. The ionizing products generated by the ^{10}B (n,α)^{7}Li capture reaction, shown in eq. (1.1), are a critical factor in detector's design. Given that ^{10}B has a relatively large neutron capture cross section of 3870 b for 25 meV [5] and about 19% natural abundance [23], one

of its compounds, $^{10}B_4C$, is particularly interesting for our purposes, considering it also presents good wear resistance besides chemical and thermal stability [24].

$$n + {}^{10}B \longrightarrow \begin{cases} {}^{7}Li\,(840\,keV) + {}^{4}He\,(1470\,keV) + \gamma\,(480\,keV)(94\%) \\ {}^{7}Li\,(1015\,keV) + {}^{4}He\,(1775\,keV)(6\%)\,. \end{cases} \tag{1.1}$$

This prototype can be easily assembled and offers the possibility to cover large areas, an essential requirement for some applications. The detector was tested in the IEA-R1 nuclear research reactor [25], at the Nuclear and Energy Research Institute (IPEN) in São Paulo, Brazil, using a monochromatic thermal neutron beam. Its versatility resulted from quickly obtaining neutron position sensitivity using a few electronics channels and presenting gain stability.

2 Experimental setup

Our double-GEM detector is composed of a stack with a 0.5 mm thick aluminum cathode coated with amorphous enriched boron carbide ($^{10}B_4C$), followed by two GEM foils, provided by CERN.

The deposition of the $^{10}B_4C$ film on the Al cathode was done by direct-current magnetron sputtering in ESS Linköping Detector Coatings Workshop, located at Linköping, Sweden. The facility is equipped with an industrial deposition unit (CC800/9, CemeCon AG) and has been dedicated to the development and production of B_4C coatings as the solid converting layers in neutron detectors. Details about the deposition machine and characterization of the B_4C thin films for neutron detectors can be found in [24, 26, 27].

In this work, two $^{10}B_4C$ targets (^{10}B enrichment > 95 wt.%) were installed on sputtering cathodes in the deposition machine. The Al plate was attached to another Al backing plate to achieve $^{10}B_4C$ coating on only one surface, where the whole assembly was mounted to an electrically grounded sample table (see figure 1). The system was first pumped down to a primary vacuum pressure of 1.5×10^{-4} Pa (1.1×10^{-6} Torr) while the Al plate was heated up to 280°C for 3 h mainly to remove the water residuals on the surfaces. After an additional 2 h cooling, the plate was then treated with radio frequency plasma etching in 0.35 Pa of pure Ar to improve the coating's adhesion by removing native oxides on the substrate surface and increasing surface roughness. Thereafter, the system was filled up with 0.8 Pa (6 mTorr) of Ar before the beginning of the $^{10}B_4C$ deposition. During the deposition, the sample table was continuously rotated to obtain a better thickness uniformity. A polished Si reference was mounted at an equivalent position of the Al plate in the same deposition run for thickness measurement of the coating and the thickness of $^{10}B_4C$ coating was measured to be approximately 2.2 µm by a profilometer (DektakXT, Bruker).

In addition to the deposition of the converter layer, the geometrical disposition of the elements within the detector is a key factor regarding the signal we want to measure. The drift, transfer, and induction regions of our prototype are represented in figure 2. The drift region has 2 mm thickness and is biased with 100 V, while the transfer and induction regions have both 1 mm thickness and are biased with 300 V and 400 V, respectively. The detector works under an open flow of an Ar/CO_2 (90/10) gas mixture, with a flow of 6 L/h through the 0.85 L volume aluminum chamber. The readout plane, produced at CERN, consists of 256+256 strips in X and Y directions, covering a 100 cm^2 sensitive area.

2022 JINST 17 P09018

Figure 1. The assembly of the Al cathode plate (highlighted with the dotted box) on the Al backing plate for deposition.

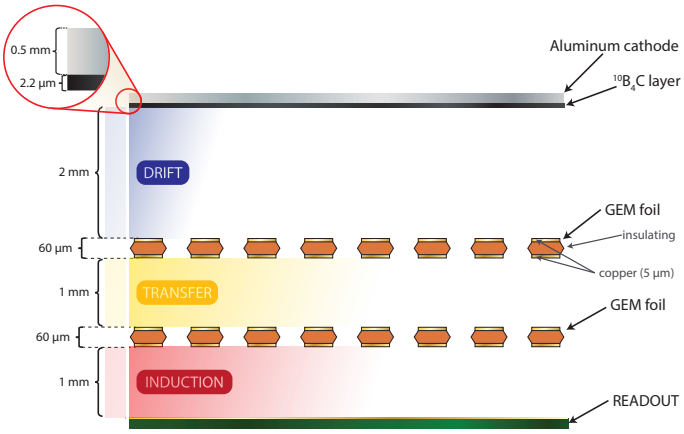

Figure 2. Detector scheme, showing the drift, transfer and induction regions. Not to scale. Figure adapted from [28].

The thickness of the drift region determines the detector's sensitivity to background gamma rays. In this context, a common requirement for thermal neutron detectors is to be insensitive to these gammas. Preliminary tests comparing 20 mm and 2 mm drift regions have shown that the latter detected five times fewer background events (approximately 3 Hz), measured with the neutron beam shutter closed. The share of events within the background range varied from 56% for the 20 mm drift region to 18% for the 2 mm region. These tests were taken into account to determine the current 100 keV threshold, which allows the detector to operate above the gamma contamination region. Therefore, we operated the detector using the 2 mm drift region, which is possible because the reaction products' high ionization power generates a large number of primary electrons. That way, even a tiny segment of their tracks is enough to provide a significant signal.

The signal multiplied by the GEM stack is collected by 256+256 strips, which are interconnected by a resistive chain composed of 60 Ω Surface Mount Device (SMD) resistors with 0.1% precision, as shown in figure 3. There are five signals collected to reconstruct a neutron image: two signals for

2022 JINST 17 P09018

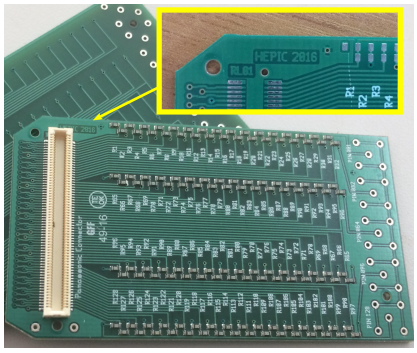

Figure 3. Printed Circuit Board (PCB) resistive chain to fit the detector signal output. Each board has 128 SMD resistors and a PANASONIC® 130-pin connector. Since the readout has 256 strips for each direction, two plates are used for each direction. Figure from [29].

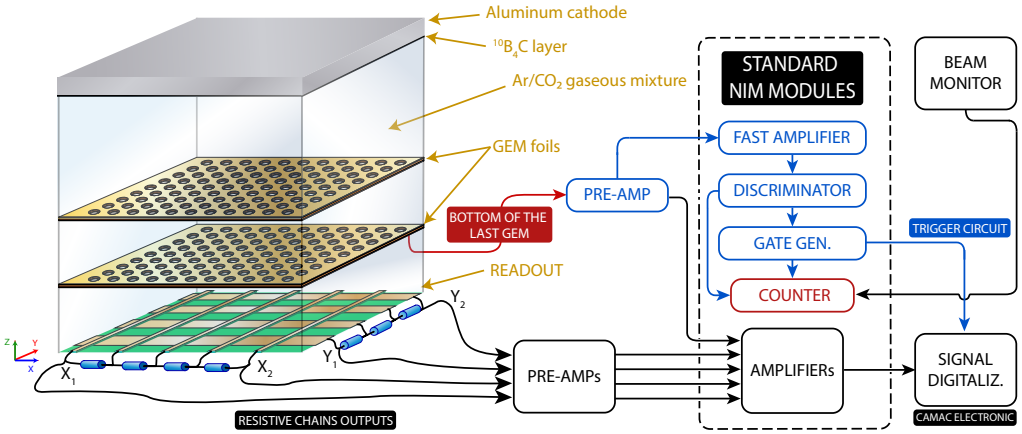

Figure 4. Signal acquisition setup scheme. The trigger circuit is pictured in blue. Figure adapted from [28].

the X direction, two for the Y direction and the charge signal, collected from the bottom electrode of the last GEM. The charge signal is used as the trigger for the data acquisition, as shown in figure 4, since it is position-independent, coming directly from the multiplication. Considering the expected extraction efficiency ϵ_{ext} for the last GEM [29], the charge signal collected at its bottom is given by $1 - \epsilon_{\text{ext}}$, which is approximately 64% of the multiplied charge for our configuration.

In order to reconstruct the event's position, we use eq. (2.1) [18], where Q is the charge information collected from the bottom of the last GEM, and L_x and L_y are the lengths of the sensitive area for each direction. As indicated in figure 4, X_1 and X_2 are the signals collected at each end of the resistive chain in the X direction, while Y_1 and Y_2 are the equivalent signals in the Y direction.

$$X_* = L_x \frac{X_2 - X_1}{Q} \qquad Y_* = L_y \frac{Y_2 - Y_1}{Q} \,. \tag{2.1}$$

As mentioned before, the detector was tested at the IEA-R1 nuclear reactor using the same neutron beam of the AURORA diffractometer [30] (see figure 5). This monochromatic neutron beam is selected out of a collimated radial neutron beam from the core of the reactor, which operates at 4.5 MW. A multi-blade focusing silicon monochromator is used to select these neutrons with

2022 JINST 17 P09018

a fixed wavelength of 1.399 Å (41.80 meV) providing a $(6.22 \pm 0.19) \times 10^4$ n cm^{-2}s^{-1} flux (ϕ), measured by the Nuclear Metrology Laboratory at IPEN with the ^{197}Au$(n, \gamma)^{198}$Au reaction, using a 12 mm diameter thin gold foil, centered at the beam outlet (letter E of figure 5).

The detector (letter A of figure 5) and the preamplifiers' box (letter C of figure 5) were mounted over an aluminum plate. This setup was fixed to a X-Y-Z precision table, that allowed the fine tuning of the detector's position with respect to the beam.

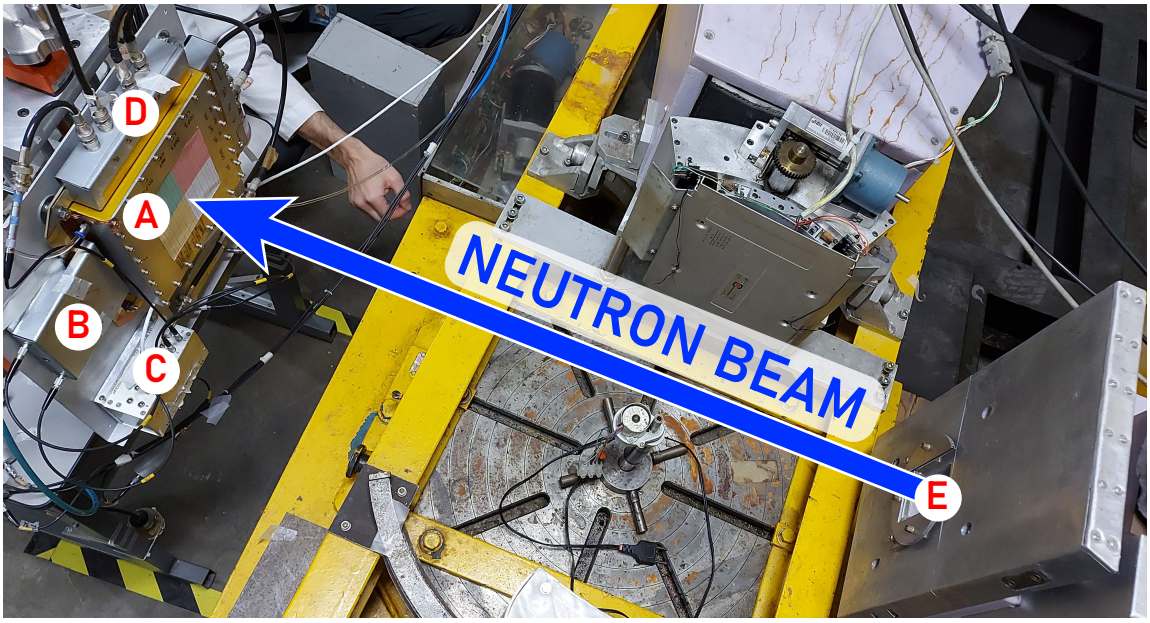

Figure 5. Position of the detector (A) relatively to the beam. The following elements are also indicated: ground shielding of the y-direction resistive chains (B), preamplifiers box (C), high voltage inputs (D), and the beam outlet (E).

3 Results and discussion

In this section, we present the main experimental results concerning the characterization of the detector: the spatial resolution obtained by two different methods, the detector efficiency, and the gain stability. We also discuss how these results relate to the previous expectations obtained with simulations.

3.1 Position calibration and resolution

To perform the spatial calibration of the detector, we used handmade cadmium masks which has a high neutron absorption cross section. Holes of different diameters were drilled in three masks. The positions and areas of the holes were measured using an image obtained with a table scanner. One of the produced masks in shown in figure 6, with its 15 holes, and its neutron image, obtained with the mask centered with respect to the detector's sensitive area.

The calibration is given by a linear dependency between the coordinates of certain holes in arbitrary units and their coordinates in known distances. The chosen holes are colinear in the X

2022 JINST 17 P09018

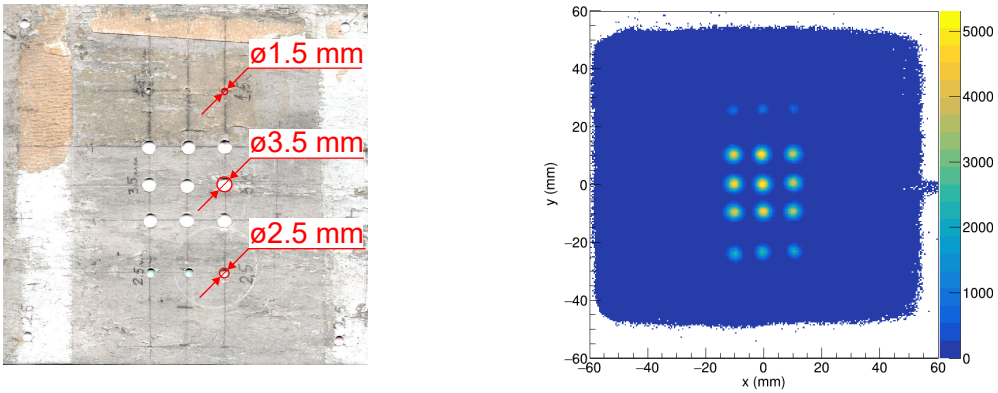

Figure 6. Left: digital image of the mask obtained with a table scanner. Right: calibrated neutron image.

and Y directions, normally the ones in the central column for Y direction and the central row for X direction. We measured the detector spatial resolution by two methods: edge and point spread functions. The first one consists of using edges to fit step functions, as shown in figure 7.

The data was fitted with the complementary error function

$$\mathrm{erfc}(p) = 1 - \frac{2}{\sqrt{\pi}} \int_0^p e^{-t^2} dt, \tag{3.1}$$

where

$$p(x) = \frac{x - \mu}{\sqrt{2}\sigma}. \tag{3.2}$$

This function provides the same parameters of interest (σ and μ) as the edge spread function (ESF). In this work, we define the position resolution as the full width at half maximum (FWHM) of the Gaussian (or the 10-to-90% distance of the ESF), i.e., 2.35σ.

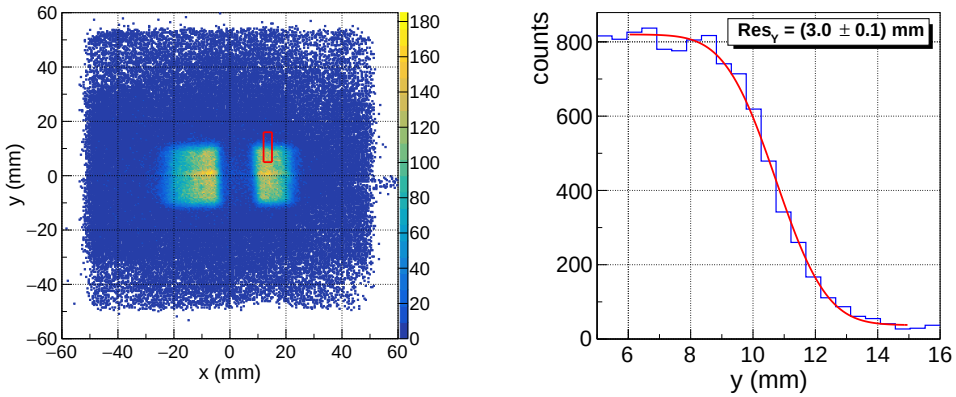

Figure 7. Left: neutron image of one of the masks, with a selected region of an edge marked as the red rectangle. Right: complementary error function (erfc) adjusted in the y-projection of the chosen area, the spatial resolution obtained is (3.0 ± 0.1) mm. Figure adapted from [28].

We measured the position resolution with the edge spread function in different regions of the detector's sensitive area and along X and Y coordinates. The results are shown in figure 8.

2022 JINST 17 P09018

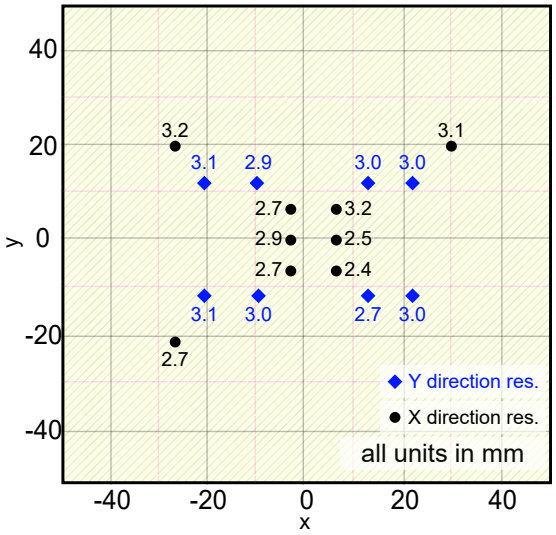

Figure 8. The points where the spatial resolution was measured using the edge spread function. The set of spatial resolution values resulted in an average value of (2.8 ± 0.3) mm for the X direction and (3.0 ± 0.1) mm for the Y direction, compatible with each other. We considered the uncertainties of the average spatial resolution for each direction as the standard deviation of each set (X and Y). Consequently, it is reasonable to consider the detector's resolution as the average of the resolutions for both directions, which results (2.9 ± 0.2) mm.

The second method relies on the fact that the FWHM of an ideally punctual hole converges to the spatial resolution of the detector, which is the FWHM of the point spread function (PSF). The projection P_{meas} obtained for a hole with a given diameter is the convolution of the PSF, for which it is safe to assume a 2D Gaussian function, with the projection of a circular area. This projection over the X direction can be written as

$$P_{\text{meas}}(x) = (P_x \circledast g)(x) := \int_{-\infty}^{\infty} f(\tau) g(x - \tau, \sigma) d\tau, \tag{3.3}$$

where g is the Gaussian function and P_x the projection of a circular area over the X direction. Fitting this convolution for holes of several diameters allows us to estimate the spatial resolution. The convolution shown in eq. (3.3) is computed numerically and the fit[1] is done using the Least Square Method. The result is shown in figure 9.

Although compatible with the 3 mm obtained with the ESF, the values obtained with this method are slightly better. This can be explained by the fact that the FWHM assigned to each diameter is the average of the FWHM for several runs using holes of that diameter.

The values obtained with the two different techniques result in a spatial resolution compatible with at least 3 mm. This spatial resolution is compatible with the obtained by similar detectors [21, 22] and is mostly limited by the fact that our detector uses only five electronic channels, which inherently only allows the estimation of the centroid of the track's charge distribution, which is at a certain distance from the neutron capture position. This distance is minimized when the maximum length of the track is truncated, such as in the case of 2 mm drift. It would be possible to strongly

[1]The fitted parameter is the resolution itself, since it is linearly dependent on σ.

2022 JINST 17 P09018

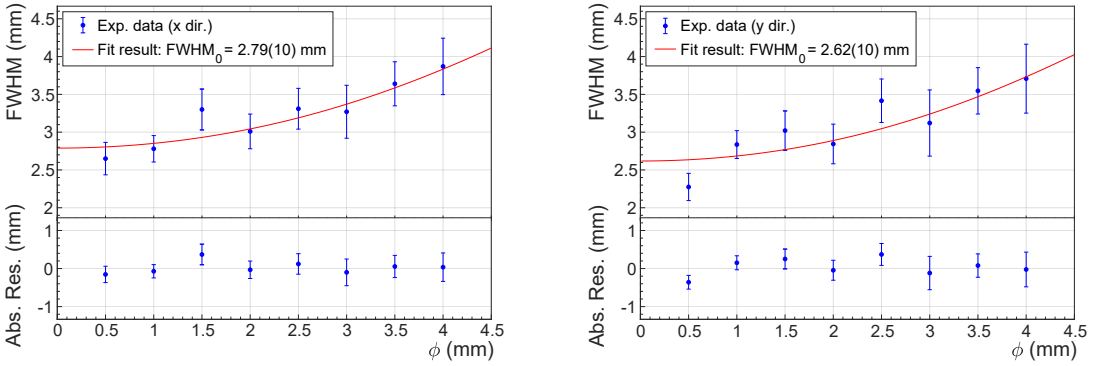

Figure 9. Convolution fit for holes with different diameters, resulting in the spatial resolution in the X (left) and Y (right) directions. We also present the absolute residuals (Abs. Res.), i.e. the difference between the experimental data and the fit, for each plot. Figures adapted from [28].

enhance the spatial resolution by operating the detector in the μTPC mode (such as in [31]), however, it would be necessary to use a much more sophisticated acquisition system.

3.2 Detector efficiency and gain stability

3.2.1 Analytic calculation

It is possible to obtain the expected detection efficiency ε_d from analytical calculations. The first step is to compute the capture efficiency ε_c, which depends on the macroscopic cross-section Σ for the converter material and its thickness $d = (2.2 \pm 0.1)\,\mu\text{m}$, where the uncertainty should comprise eventual irregularities of the deposition process. Taking the converter ($^{10}B_4C$) density $\rho = 2.3\,\text{g cm}^{-3}$ [32], its neutron capture cross section for 41.8 meV neutrons $\sigma = (2994 \pm 9)\,\text{b}$ [5], its molar mass $M_{B_4C} = 52\,\text{g mol}^{-1}$, and the stoichiometry a of ^{10}B in a $^{10}B_4C$ converter layer, which is 4, one can obtain the number of target nuclei of the converter:

$$N = a\frac{\rho}{M}N_A = 1.065 \times 10^{23}\,\text{cm}^{-3}. \tag{3.4}$$

The result of eq. (3.4) is used to compute the macroscopic cross-section [33] for the converter layer:

$$\Sigma = N\sigma = (3.19 \pm 0.01) \times 10^{-2}\,\mu\text{m}^{-1}. \tag{3.5}$$

The neutron beam intensity after crossing our converter layer is

$$I_{\text{beam}} = e^{-\Sigma d} = (93.2 \pm 0.3)\%. \tag{3.6}$$

Therefore, the capture efficiency is given by the percentage of absorbed neutrons:

$$\varepsilon_c = 1 - e^{-\Sigma d} = (6.8 \pm 0.3)\%. \tag{3.7}$$

When the neutron is captured too far from the lower side of the converter layer (at the boundary with the gaseous region), it might not be detected because the products of the capture reaction do not have enough energy to exit the layer, as pictured in figure 10 (case A). Therefore, such products have to fulfill a set of geometrical requisites that depend on the capture's position, which are shown

2022 JINST 17 P09018

in figure 10 (case B and C). Finally, the products that enter the drift region with too low energy are also not detected since there is an energy threshold to handle electrical noise and other acquisition system specifications.

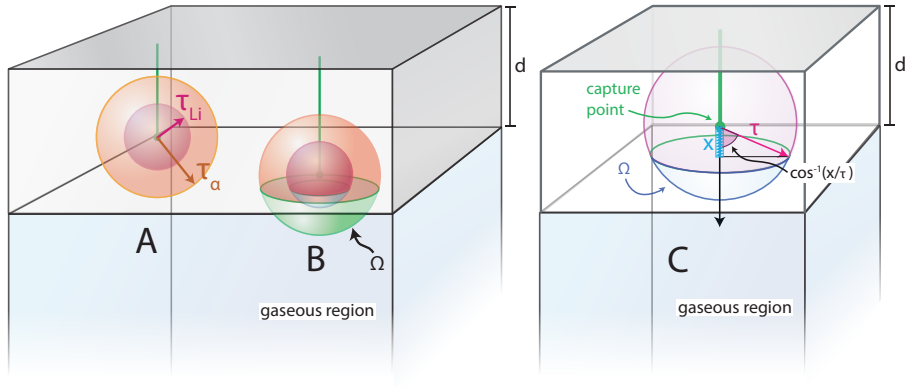

Figure 10. The spheres of radius τ_α and τ_{Li} define the accessible region for the α and ^{7}Li nuclei, respectively, inside the converter layer (A). Given certain capture point, only the products within the solid angle Ω reaches the gas (B). The solid angle Ω is a function of the angle $\cos^{-1}(x/\tau)$, where x is the smallest distance between the capture point and the drift region (C). Figure adapted from [28].

In order to account for the constrains discussed above, the values for τ_α and τ_{Li}, for both possible decay channels of eq. (1.1), were evaluated from direct integration of the average dE/dx plot generated through SRIM [34]. It is also necessary to consider the energy threshold, which was done by finding τ for which the average remaining energy for the given particle is equal to the threshold used in the experiment, of (100 ± 10) keV. This process is shown in figure 11.

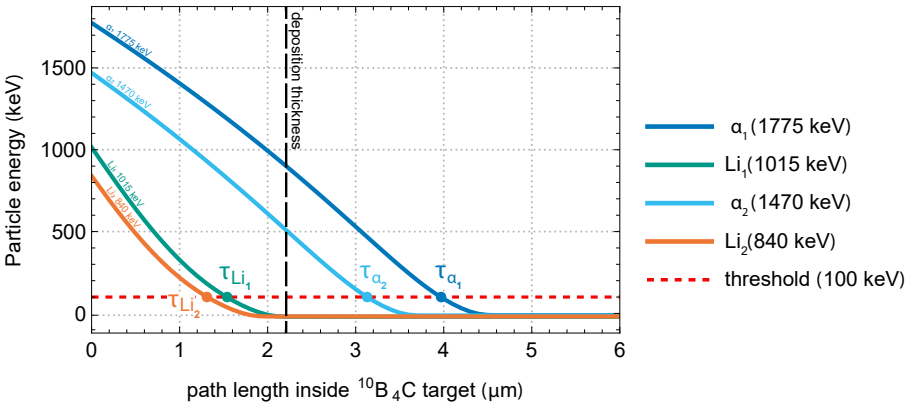

Figure 11. Remaining energy for each ^{10}B (n,α)^{7}Li reaction product as a function of depth for a theoretically infinite $^{10}B_4C$ converter layer. The τ values used for the calculations are the depth at which the particle's remaining energy equals the threshold. This condition gives: $\tau_{\alpha_1}(1775\,\mathrm{keV}) = 3.97\,\mu\mathrm{m}$, $\tau_{\alpha_2}(1470\,\mathrm{keV}) = 3.13\,\mu\mathrm{m}$, $\tau_{\mathrm{Li}_1}(1015\,\mathrm{keV}) = 1.54\,\mu\mathrm{m}$ and $\tau_{\mathrm{Li}_2}(840\,\mathrm{keV}) = 1.31\,\mu\mathrm{m}$.

2022 JINST 17 P09018

The considerations above are translated to the calculation for the detection efficiency ε_d as follows:

$$\varepsilon_d = F\varepsilon_c = F\left(1 - e^{-\Sigma d}\right), \tag{3.8}$$

where F is the share of capture products emitted within the solid angle Ω of figure 10(B), and is computed as

$$F = \sum_{\text{all products}} F(d, \tau_i) = \sum_{\tau_i = \tau_{\alpha_1}, \tau_{\alpha_2}, \tau_{\text{Li}_1}, \tau_{\text{Li}_2}} \int_0^d \int_0^{\cos^{-1}(x/\tau_i)} d\Omega dx \approx 0.477, \tag{3.9}$$

for a boron carbide layer of thickness 2.2 µm, where τ_i are the path length for each product: τ_{α_1} = 3.97 µm, τ_{α_2} = 3.13 µm, τ_{Li_1} = 1.54 µm and τ_{Li_2} = 1.31 µm. As result, we obtain the neutron detection efficiency

$$\varepsilon_d = (3.22 \pm 0.14)\,\%. \tag{3.10}$$

3.2.2 Simulations

Monte Carlo simulations play an important role in the development and optimization of this kind of detector. For this purpose, GEANT4 is a powerful tool to describe the detector and for the simulation of the interaction of particles with matter [35], allowing the simulation of the nuclear reaction, like eq. (1.1), as well as the transport of the reaction products inside the detector.

The detector was simulated with GEANT4 using the physics list *QGSP_BERT_HP* (which has high precision models for low energy neutrons [36]), according to the device described in section 2. The simulation consisted in a parallel uniform beam with 10^6 neutrons of 1.399 Å (41.80 meV), hitting the detector in a direction perpendicular to the converter layer.

Taking 14 different thicknesses ranging from 0.25 µm to 5 µm of the boron carbide converter layer, we evaluate the thermal neutrons detection efficiency by counting the charged particles that leave the boron converter and reach the gaseous volume. For a nominal thickness of 2.2 µm, an efficiency of

$$(3.14 \pm 0.10)\%$$

was obtained. While the maximum efficiency was achieved with a thickness of 2.5 µm resulting in $(3.17 \pm 0.10)\%$, as shown in figure 12. We did not considered the experimental threshold (100 keV) when evaluating the theoretical efficiency in this case.

Using the low-energy electromagnetic model Livermore [36], we simulated the deposited energy by the reaction products inside the 2 mm of the drift region. This simulation is used as an energy pre-calibration for the experimental spectrum since both present the same primary structure, consisting of an energy peak around 600 keV, as shown in figure 13. We did not include the experimental energy threshold (100 keV) of our system nor the charge multiplication process in the simulation, which means considering that the acquired energy is equal to the energy deposited by the reaction products in the absorption region of the detector.

3.2.3 Experimental measurements

The detection efficiency is evaluated by dividing the number of detected neutrons N_{det} by the total number of neutrons N_{tot} hitting the detector. We calculated the total number of neutrons from the

2022 JINST 17 P09018

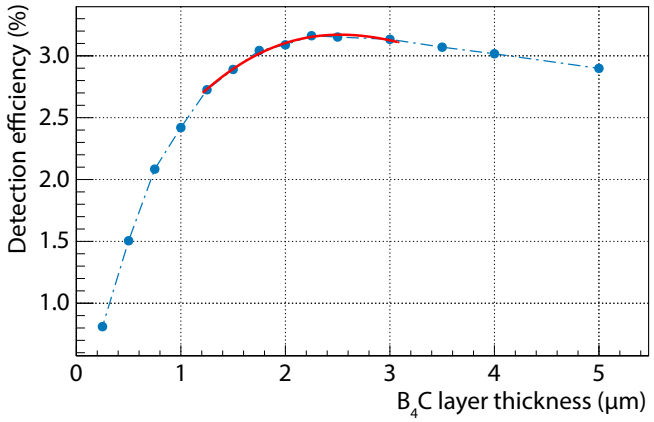

Figure 12. Detection efficiency for one layer of boron carbide, simulated with GEANT4. The fit for maximum efficiency is an arbitrary function adjusted just to guide the eye within the interval that comprises the data around the peak (continuous line).

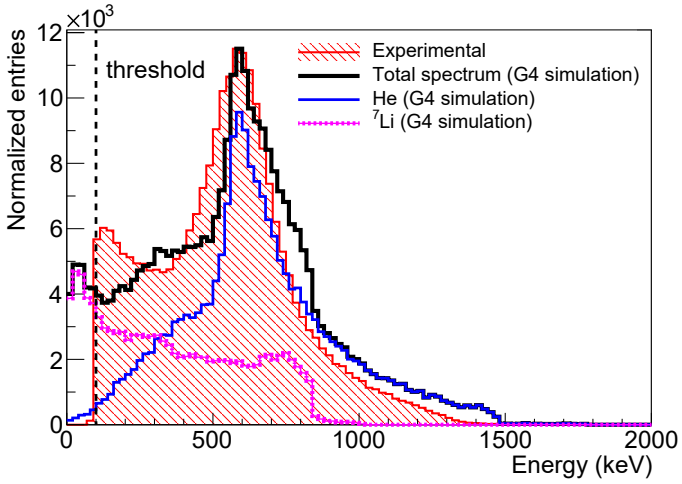

Figure 13. Experimental energy spectrum compared with the GEANT4 simulation. The simulation does not include the effect of the detector finite energy resolution and was normalized to the maximum counts of the experimental energy spectrum. Figure from [28].

neutron flux ϕ, measured as described in section 2, the area A selected from the beam and the time length Δt of the measurement. The neutron flux was corrected using the counts of a fission chamber installed at the neutron beam outlet using as reference the number of counts registered by this same chamber during the neutron flux calibration process. With these values, the experimental neutron detection efficiency is given by

$$\varepsilon = \frac{N_{\text{det}}}{N_{\text{tot}}} = \frac{N_{\text{det}}}{\phi A \Delta t}. \tag{3.11}$$

Using cadmium masks with squared holes, we selected different areas from the beam: 0.36 cm^2 and 1.44 cm^2, at the same position where the flux measurement was taken. The total number of detected neutrons N_{det} was counted with negligible uncertainties at these rates. We obtained

2022 JINST 17 P09018

(2.75 ± 0.26)% detection efficiency for the 0.36 cm^2 mask and (2.57 ± 0.15)% for the 1.44 cm^2, which are compatible within 1 σ with each other.

The gain stability was monitored in real-time, in order to provide necessary corrections to the image reconstruction in offline data analysis. A gain shift would imply changes in efficiency since the energy spectrum would be displaced from its original position with respect to the energy threshold. Besides that, changes in the gain over time may bring the detector to an unstable operation in terms of discharge probability.

The data shown in figure 14 present a method to analyze the gain stability: the energy channel of the run was divided into batches of 4 min each (separated by the dashed vertical lines) and plotted over time. Then, we locate the spectrum peak using a peak identification algorithm [37] and fit a Gaussian to it, registering its center as the cross marker in figure 14. Slow gain changes due to environmental changes are easily seen as a tendency in the sequence of the points, whose energy spectrum can be drifted by a reasonable amount as it happens in the case reported by [18]. The tendency analysis can be carried out by fitting the behaviour of the difference between each peak position and the average position of all peaks, which we labelled as Δ_{peak} in the figure 14.

There is a slight drift of the spectrum's peak within about 2.5 h, as the fit result of figure 14 suggests. However, this drift is smaller than 10 ADC channels, corresponding to about 0.2% h^{-1} change, which is not statistically sufficient to be interpreted as a reasonable change. Also, at the beginning of the operation, some slow gain stabilization of these detectors are expected, as reported in other works [38–42]. The monitoring remains essential since it can be used to correct the detector's efficiency if significant changes happen, using the detector's current rate and the neutron monitor fission chamber.

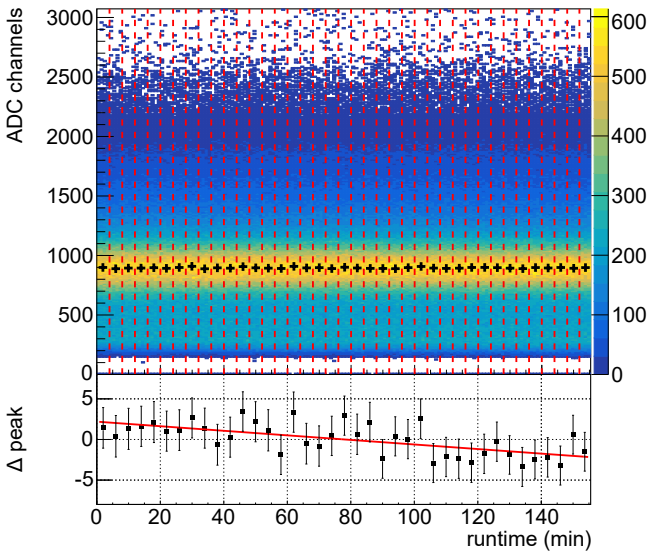

Figure 14. Temporal stability analysis with the tendency analysis. This run has 4793145 events and was divided into batches of 4 min (123 403 entries each), generating 39 peaks. The average of the peak position was 897 ± 2 ADC channels. The fit for Δ_{peak} resulted an angular coefficient −0.028 ± 0.009 ADC channel/min and a linear coefficient equals to 2.2 ± 0.8 ADC channels.

2022 JINST 17 P09018

4 Final considerations

A neutron detector was built with a single boron carbide layer and a resistive charge division readout. This detector shows the feasibility of a position-sensitive detector that can be easily mounted in a neutron beam line based on simple standard electronics. The detector also operates above of the background gamma rays sensitive region (registering no events when the neutron beam is off), an essential feature for its use in environments like nuclear reactor research facilities. If needed, the gamma sensitivity can be controlled by changing the drift region, and a new energy pre-calibration can be quickly obtained with new simulation results.

The average of the obtained thermal neutron detection efficiency is $(2.66 \pm 0.15)\%$, which agrees within 2.7 σ with the prediction of $(3.22 \pm 0.14)\%$ and with the preliminary simulation of $(3.14 \pm 0.10)\%$, and can be reduced by altering the layer thickness allowing different applications, such as beam monitors. At the current configuration, one can use the detector to measure the beam profile given that the position resolution obtained was at least 3 mm. There is also the possibility to raise the efficiency by adding new converter layers over the GEMs, as seen in other works [19, 20, 43]. For future works and following that same idea, it is possible to use boron coated Thick-GEMs, operating with unitary effective gain, raising the thermal neutron detection efficiency.

Acknowledgments

This work was supported by CNPq grant 156767/2019-8.
H. Natal da Luz acknowledges project GAČR GA21-21801S (Czech Science Foundation).
This work was partially supported by grant #2012/04583-8, São Paulo Research Foundation (FAPESP).

References

[1] A. Pietropaolo et al., *Neutron detection techniques from μeV to GeV*, *Phys. Rept.* **875** (2020) 1.

[2] R. Hall-Wilton and C. Theroine, *Status of the European Spallation Source ESS AB, the Instrument Selection Process, and a Fundamental Physics Beamline at the ESS*, *Phys. Procedia* **51** (2014) 8.

[3] X. Ledoux et al., *First beams at neutrons for science*, *Eur. Phys. J. A* **57** (2021) 257 [arXiv:2110.02282].

[4] B. DiGiovine et al., *A holistic approach to the optimization of neutron beam transport at the LANSCE facility*, *Nucl. Instrum. Meth. A* **1013** (2021) 165631.

[5] A.J. Koning, D. Rochman, J.C. Sublet, N. Dzysiuk, M. Fleming and S. van der Marck, *TENDL: Complete Nuclear Data Library for Innovative Nuclear Science and Technology*, *Nucl. Data Sheets* **155** (2019) 1.

[6] R.T. Kouzes, *The ^{3}He supply problem*, U.S. Department of Energy, Oak Ridge, TN, U.S.A. (2009) [PNNL-18388] and online pdf version at https://www.pnnl.gov/main/publications/external/technical_reports/PNNL-18388.pdf.

[7] F. Sacchetti et al., *^{3}He-free neutron detectors and their applications*, *Eur. Phys. J. Plus* **130** (2015) 53.

[8] A. Miyake, T. Nishioka, S. Singh, H. Morii, H. Mimura and T. Aoki, *A CdTe detector with a Gd converter for thermal neutron detection*, *Nucl. Instrum. Meth. A* **654** (2011) 390.

2022 JINST 17 P09018

[9] A. Pietropaolo et al., *A new ^{3}He-free thermal neutrons detector concept based on the GEM technology*, *Nucl. Instrum. Meth. A* **729** (2013) 117.

[10] E.M. Schooneveld et al., *Radiative neutron capture as a counting technique at pulsed spallation neutron sources: a review of current progress*, *Rept. Prog. Phys.* **79** (2016) 094301.

[11] A. Compaan et al., *Thin-film neutron detector based on CdTe and ^{6}Li layers*, *Nucl. Instrum. Meth. A* **954** (2020) 161127.

[12] G. Albani et al., *High-rate measurements of the novel BAND-GEM technology for thermal neutron detection at spallation sources*, *Nucl. Instrum. Meth. A* **957** (2020) 163389.

[13] F. Sauli, *GEM: A new concept for electron amplification in gas detectors*, *Nucl. Instrum. Meth. A* **386** (1997) 531.

[14] ALICE collaboration, *Upgrade of the ALICE Time Projection Chamber*, CERN-LHCC-2013-020 [ALICE-TDR-016] (2013).

[15] C. Altunbas et al., *Construction, test and commissioning of the triple-GEM tracking detector for COMPASS*, *Nucl. Instrum. Meth. A* **490** (2002) 177.

[16] D. Abbaneo et al., *Overview of large area triple-GEM detectors for the CMS forward muon upgrade*, *Nucl. Instrum. Meth. A* **845** (2017) 298.

[17] K. Gnanvo et al., *Detection and imaging of high-z materials with a muon tomography station using GEM detectors*, in proceedings of the *IEEE Nuclear Science Symposuim and Medical Imaging Conference*, Knoxville, TN, U.S.A., 30 October–6 November 2010, IEEE, New York, NY, U.S.A. (2010), pp. 552–559.

[18] G.G.A. de Souza and H.N. da Luz, *XRF element localization with a triple GEM detector using resistive charge division*, *Nucl. Instrum. Meth. A* **937** (2019) 141 [arXiv:1901.02849].

[19] M. Klein and C.J. Schmidt, *Cascade, neutron detectors for highest count rates in combination with ASIC/FPGA based readout electronics*, *Nucl. Instrum. Meth. A* **628** (2011) 9.

[20] M. Köhli et al., *Efficiency and spatial resolution of the cascade thermal neutron detector*, *Nucl. Instrum. Meth. A* **828** (2016) 242.

[21] J. Zhou et al., *Highly efficient gem-based neutron detector for china spallation neutron source*, *Nucl. Instrum. Meth. A* **953** (2020) 163051.

[22] J. Zhou et al., *A sealed ceramic gem-based neutron detector*, *Nucl. Instrum. Meth. A* **995** (2021) 165129.

[23] M. Berglund and M.E. Wieser, *Isotopic compositions of the elements 2009 (IUPAC technical report)*, *Pure Appl. Chem.* **83** (2011) 397.

[24] S. Schmidt, C. Höglund, J. Jensen, L. Hultman, J. Birch and R. Hall-Wilton, *Low-temperature growth of boron carbide coatings by direct current magnetron sputtering and high-power impulse magnetron sputtering*, *J. Mater. Sci.* **51** (2016) 10418.

[25] J. Perrotta, L. Terremoto and C. Zeituni, *Experience on wet storage spent fuel sipping at IEA-R1 Brazilian research reactor*, *Ann. Nucl. Energy* **25** (1998) 237.

[26] C. Höglund et al., *B_4C thin films for neutron detection*, *J. Appl. Phys.* **111** (2012) 104908.

[27] C. Höglund et al., *Stability of $^{10}B_4C$ thin films under neutron radiation*, *Radiat. Phys. Chem.* **113** (2015) 14.

2022 JINST 17 P09018

[28] L.A. Serra Filho, *Gem-based thermal neutron detector with $^{10}B_4C$ deposition on aluminum cathode*, Master's Thesis, Universidade de São Paulo, São Paulo, Brazil (2021) [https://doi.org/10.11606/D.43.2022.tde-08032022-102912].

[29] G.G.A. de Souza, *X-ray fluorescence imaging system based on Thick-GEM detectors*, Master's Thesis, Universidade de São Paulo, São Paulo, Brazil (2019) [https://doi.org/10.11606/D.43.2019.tde-21032019-233121].

[30] C. Parente, V. Mazzocchi, J. Mestnik-Filho, Y. Mascarenhas and R. Berliner, *Aurora — a high-resolution powder diffractometer installed on the IEA-R1 research reactor at IPEN-CNEN/SP*, *Nucl. Instrum. Meth. A* **622** (2010) 678.

[31] D. Pfeiffer et al., *First Measurements with New High-Resolution Gadolinium-GEM Neutron Detectors*, 2016 *JINST* **11** P05011 [arXiv:1510.02365].

[32] C. Höglund et al., *B_4C thin films for neutron detection*, *J. Appl. Phys.* **111** (2012) 104908.

[33] E.M. Hussein, *Mechanisms*, in *Radiation Mechanics. Principles and Practice*, E.M. Hussein ed., Elsevier Science, Amsterdam, The Netherlands (2007), chapter one, pp. 1–65.

[34] J.F. Ziegler, M. Ziegler and J. Biersack, *Srim — the stopping and range of ions in matter (2010)*, *Nucl. Instrum. Meth. B* **268** (2010) 1818.

[35] GEANT4 collaboration, *GEANT4 — a simulation toolkit*, *Nucl. Instrum. Meth. A* **506** (2003) 250.

[36] GEANT4 collaboration, *Geant 4 — Physics Reference Manual. Release 10.7. Rev5.0*, (2020) and online pdf version at http://cern.ch/geant4-userdoc/UsersGuides/InstallationGuide/BackupVersions/V10.7/fo/Geant4InstallationGuide.pdf.

[37] M. Morháč, J. Kliman, V. Matoušek, M. Veselský and I. Turzo, *Identification of peaks in multidimensional coincidence gamma-ray spectra*, *Nucl. Instrum. Meth. A* **443** (2000) 108.

[38] S. Chatterjee, A. Sen, S. Das, S. Ghosh and S. Biswas, *Study of charging-up effect for a single mask triple GEM detector*, *Nucl. Instrum. Meth. A* **1014** (2021) 165749.

[39] S. Chatterjee et al., *Study of charging up effect in a triple GEM detector*, 2020 *JINST* **15** T09011 [arXiv:2007.11444].

[40] P. Hauer et al., *Measurements of the charging-up effect in gas electron multipliers*, *Nucl. Instrum. Meth. A* **976** (2020) 164205.

[41] M. Alfonsi et al., *Simulation of the dielectric charging-up effect in a GEM detector*, *Nucl. Instrum. Meth. A* **671** (2012) 6.

[42] M. Chernyshova et al., *Effect of charging-up and regular usage on performance of the triple GEM detector to be employed for plasma radiation monitoring*, *Fusion Eng. Des.* **158** (2020) 111755.

[43] A. Muraro et al., *Mbgem: a stack of borated gem detector for high efficiency thermal neutron detection*, *Eur. Phys. J. Plus* **136** (2021) 742.

2022 JINST 17 P09018